

Article

Not peer-reviewed version

---

# GPR in Damage Identification of Concrete Elements – A Case Study of Diagnostics in a Prestressed Bridge

---

[Piotr Łaziński](#), [Marcin Jasiński](#), [Mateusz Uściłowski](#), [Dawid Piotrowski](#)<sup>\*</sup>, [Łukasz Ortył](#)

Posted Date: 12 November 2024

doi: 10.20944/preprints202411.0778.v1

Keywords: GPR; non-destructive testing; bridge; prestressed concrete structures



Preprints.org is a free multidisciplinary platform providing preprint service that is dedicated to making early versions of research outputs permanently available and citable. Preprints posted at Preprints.org appear in Web of Science, Crossref, Google Scholar, Scilit, Europe PMC.

Copyright: This open access article is published under a Creative Commons CC BY 4.0 license, which permit the free download, distribution, and reuse, provided that the author and preprint are cited in any reuse.

Disclaimer/Publisher's Note: The statements, opinions, and data contained in all publications are solely those of the individual author(s) and contributor(s) and not of MDPI and/or the editor(s). MDPI and/or the editor(s) disclaim responsibility for any injury to people or property resulting from any ideas, methods, instructions, or products referred to in the content.

Article

# GPR in Damage Identification of Concrete Elements –A Case Study of Diagnostics in a Prestressed Bridge

Piotr Łaziński <sup>1</sup>, Marcin Jasiński <sup>1</sup>, Mateusz Uściłowski <sup>1</sup>, Dawid Piotrowski <sup>1,\*</sup> and Łukasz Ortyl <sup>2</sup>

<sup>1</sup> Faculty of Civil Engineering, Silesian University of Technology, ul. Akademicka 2A, 44-100 Gliwice, Poland

<sup>2</sup> Faculty of Geo-Data Science, Geodesy, and Environmental, AGH University of Krakow, al. Mickiewicza 30, 30-059 Cracow, Poland

\* Correspondence: dawid.piotrowski@polsl.pl

**Abstract:** Effective placement and compaction of the concrete mixture within the spans of prestressed bridges are essential for the proper anchoring and prestressing of tendons. High density of reinforcement and location of the cable ducts present significant challenges, increasing the risk of void formation and structural irregularities, which can lead to failures during the prestressing process. Ground Penetrating Radar (GPR) emerges as a pivotal non-destructive testing method for diagnosing such complex prestressed structures. Utilizing high-frequency electromagnetic waves, GPR accurately detects and maps anomalies within hardened concrete, enabling precise identification of defect locations and their dimensions. The detailed imaging provided by GPR facilitates the development of targeted repair strategies and allows for the exclusion of concrete voids through selective invasive inspections in designated boreholes. This study presents the use of GPR for the investigation of anomalies and damage in prestressing tendons of a newly built concrete bridge. It underscores the critical role of GPR in enhancing the diagnostic and maintenance programs for prestressed bridge structures, thereby improving their overall integrity and longevity.

**Keywords:** GPR; non-destructive testing; bridge; prestressed concrete structures

## 1. Introduction

Concrete is one of the most widely used construction materials [1]. The casting process and the characteristics of the concrete mixture, such as mechanical and chemical properties, its composition, workability, and sustainability, are important factors for the integrity and quality of concrete [2]. This directly translates into the performance of structural elements, including prestressed concrete members [3]. Due to span lengths and load magnitude, prestressed concrete is especially common in bridge engineering, allowing for an improvement in capacity and durability [4]. The required amount of prestressing steel and reinforcement in bridges is significant, especially near joints, crossbeams, anchorages, and support zones. The high reinforcement ratio, the presence of cable ducts, as well as the size and dimensions of the elements pose a risk to the correct placement of the mixture, its compaction, distribution, and homogeneity, resulting in voids, delamination, honeycombs, bugholes, and other defects in concrete [5,6].

Diagnostics of reinforced and prestressed concrete can include destructive, semi-destructive, and non-destructive techniques [7,8], among which non-destructive tests (NDT) are of particular interest and emerging [9]. NDT embrace a variety of in-situ methods for the evaluation and assessment of material integrity and quality, along with its characteristics and properties, without destroying or affecting the structure [10].

Non-destructive testing can be categorized into five primary groups [11]: acoustic, mechanical, electromagnetic, electrochemical and optical/visual methods (Figure 1).

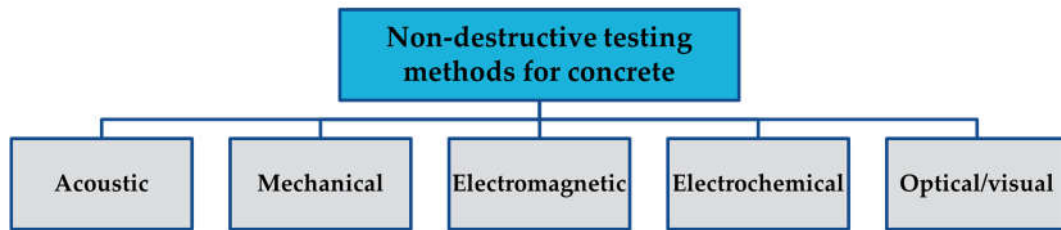


**Figure 1.** Classification of Non-Destructive Testing Methods for Concrete.

Acoustic methods are widely used to evaluate the internal structure of concrete, including the detection of cracks, voids and delamination. These methods rely on the propagation of sound waves through the material, which can reveal information about the concrete's homogeneity, density and potential defects. Examples of acoustic methods include: ultrasonic pulse velocity [12–14], acoustic emission [15,16], ultrasonic tomography [17] and impact echo [13].

Mechanical methods are primarily used to estimate the compressive strength, surface hardness and uniformity of concrete. By applying physical impacts to the surface, these techniques can provide insight into the mechanical properties of the material. They are typically easy to perform and provide quick assessments, making them a common choice for evaluating the overall condition of concrete structures, especially in the field. The most common mechanical method is the rebound hammer test [12–14], which is used to determine compressive strength, surface hardness and homogeneity.

Optical and visual methods include traditional surface inspections as well as more advanced techniques for monitoring structural behavior. These methods are mainly used to detect surface defects, such as cracks and discoloration and can also measure deformation and strain. By providing detailed visual data, they help in monitoring the structural health and detecting early signs of damage. More sophisticated optical techniques can even offer continuous monitoring, providing real-time feedback on the structural performance of concrete elements. Examples of optical methods are digital image correlation [16] and the use of optical fiber sensors [15].

Electrochemical methods are focused on evaluating the corrosion potential and rate of embedded steel reinforcement. They are crucial for assessing the durability and long-term performance of reinforced concrete structures by measuring parameters that indicate the likelihood of corrosion. These methods can provide early warning signs of deterioration, allowing for timely maintenance and repair actions. Examples of electrochemical methods include: half-cell potential test [13,14] and linear polarization resistance [18].

Electromagnetic methods, shown in Figure 2, represent the second most popular category of non-destructive testing for concrete elements, including a ground-penetrating radar (GPR) which was chosen for further consideration in this research. They work by emitting electromagnetic waves into the material, which are then reflected back, providing information on the internal structure. In addition to GPR [13,19], the following techniques are also used: infrared thermography [13,20], radiography [13,15], eddy current testing [15] and computerized tomography [16].

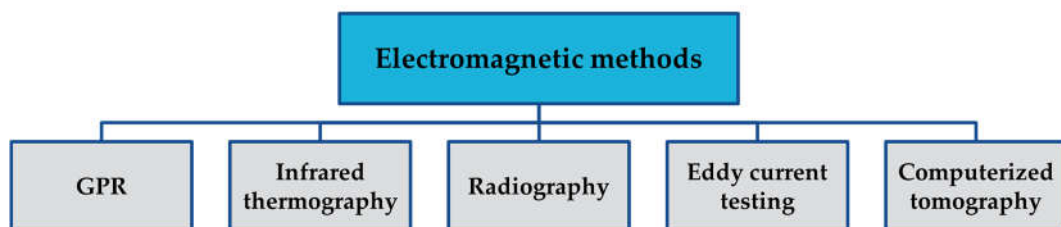


**Figure 2.** Classification of Electromagnetic Methods for Non-Destructive Testing of Concrete.

GPR is a non-destructive method for defect detection based on the reflection of microwaves near structural anomalies and inconsistencies. It has various applications in damage detection, diagnostics, condition assessment, and quality control of concrete structures [21]. It allows

examination of corrosion [22], including cracks [23], chloride migration and carbonation [24], moisture [25], and rebar corrosion [26–28]. In similar applications, GPR measurements were enriched with additional techniques and machine learning algorithms, along with artificial neural networks [29,30]. Hu et al. [31] described the augmentation of the GPR image dataset for deep learning-based identification and location of underground defects, including dry and water-bearing voids. Wong et al. [32] coupled GPR data and logistic regression for the evaluation of chloride-induced corrosion and internal cracks in concrete. Abu Dabous et al. [33] proposed a method that integrates infrared thermography and GPR to improve the detection of defects in concrete bridge decks, including subsurface delamination and moisture. Solla et al. [34] used combined infrared thermography and GPR for the assessment of rebar corrosion. Janků et al. [35] compared infrared thermography, GPR, and ultrasonic pulse echo methods for the detection of delamination in concrete bridges, concluding that GPR and ultrasonic pulse echo are better suited to locate inner defects. Yang et al. [36] made a similar comparison for the assessment of road infrastructure. Kang et al. [37] examined the detection of cavities beneath concrete plates by simultaneous GPR and the analysis of acoustic signals induced by impacting the plates with an instrumented hammer. Some literature describes the use of GPR to diagnose the cause of moisture, dampness, and water leakage in structures. Lai et al. [38] described tracking of water seepage pathway of a pipe embedded in a concrete wall. Garrido et al. [39] applied infrared thermography and GPR for the detection and classification of moisture in walls. Similarly, Buliuk et al. [40] proposed a GPR-based method for the detection of leakage and waterproofing damage on concrete bridge decks. Repeated measurements with comparison of GPR images taken at different times offer promising improvements in structural health monitoring. Following this assumption, Tasker et al. [41] used GPR to track changes in response within a concrete wall to an external load of increasing magnitude.

GPR allows for quick data acquisition and coverage of extent areas. Therefore, it is particularly suitable for investigating large-scale structures and linear infrastructure, including roads [42], railways [43], bridges [44,45], tunnels [46–48], or dams [49–51]. For example, Sun et al. [52] coupled acoustic scanning and GPR for rapid delamination mapping on bridges of different geometries. GPR was used for the detection of grouting defects in shield tunnel construction [53] or voids behind the lining structures [54].

GPR is widely used specifically for inventories and rebar positioning, for example in slabs [55], bridge decks [56], and bearing zones [57]. Lachowicz and Rucka [58] discussed the numerical and experimental identification of rebars in areas of a high reinforcement ratio. Liu et al. [59] enhanced the process of a deep convolutional neural network model. The use of GPR for inventories was also reported by Alam et al. [60] who focused on a data-driven evaluation of thickness and material type in layered structures.

Reports of the usage of GPR for the examination of newly created structures are rather limited, although the complexity of construction works and the number of environmental, economic, and social factors that can affect their quality are still causing problems [61,62]. Rasol et al. [63] combined GPR and computational modeling to identify early cracking in concrete pavements. Hasan and Yazdani [64] carried out an evaluation of concrete covers on a newly built bridge in Texas. Liu et al. [65] worked on the detection of early-stage rebar corrosion using a polarimetric GPR system. Zhao et al. [66] in turn, used GPR to estimate the thickness of the asphalt concrete overlay and its density.

To fill the gap and enhance the practical experience in GPR-based non-destructive tests of newly built prestressed concrete structures, this study describes the investigation of structural defects revealed during the construction process. The GPR method was successfully applied to investigate anomalies that were noticed during the grouting process of prestressing cables, which were further verified by semi-destructive tests, including drilling. Taking into account the general difficulties and ambiguities in interpreting the GPR output, the results presented can be especially valuable to researchers and practitioners for further interpretation of GPR signals in similar cases. The purpose of this study is to enhance the current database of GPR surveys, allowing their further use in the damage detection and identification and enabling a comprehensive evaluation of bridge structures.

## 2. Tests of Selected Bridge Elements

Based on the critical role of concrete placement and compaction in prestressed bridges, this section delves into the specific challenges posed by high-density reinforcement and the placement of cable ducts. Maintaining the appropriate consistency of the concrete mixture is paramount for effective casting and distribution. However, ensuring thorough compaction remains a significant challenge, particularly in areas such as crossbeams, anchorage blocks, and bearing zones. The dense network of intersecting reinforcement within girders and crossbeams, combined with the layout of cable ducts, substantially increases the likelihood of voids forming within the concrete elements. Consequently, failures may occur during prestressing, or improper concrete embedding may result. Examples include:

- A concrete cavity in the bottom slab of the box girder (Figure 3a);
- Near-surface voids in the bearing zone (Figure 3b);
- Insufficient compaction at the base of the pier (Figure 3c);
- Grout leaks due to inadequate sealing of the prestressing cable ducts (Figure 3d).

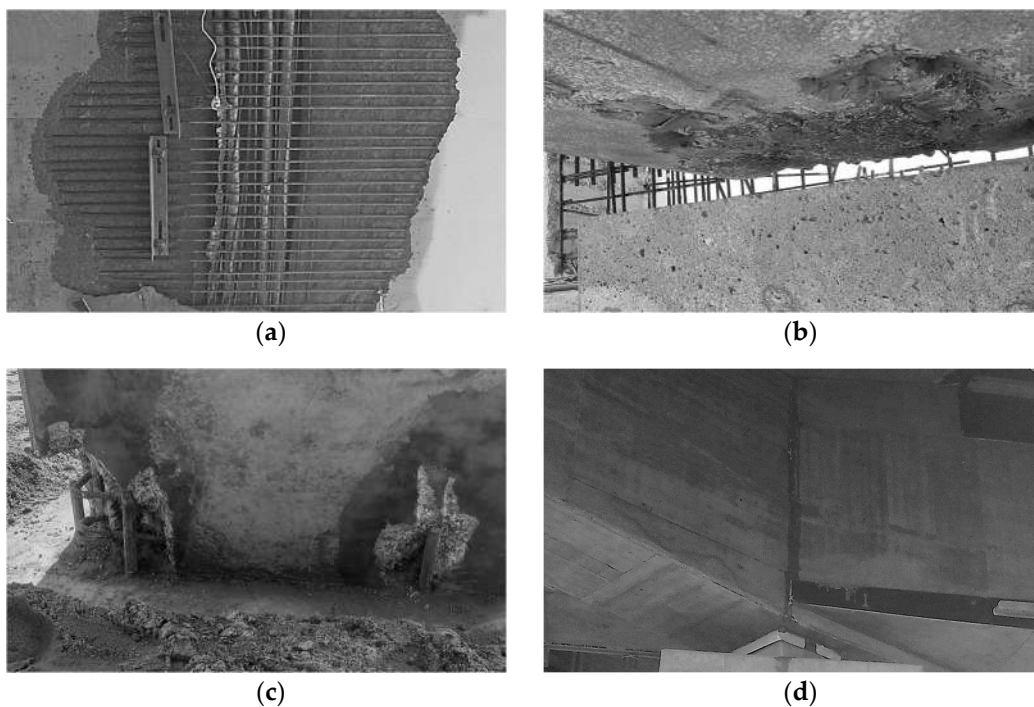


**Figure 3.** Examples of the failures during construction: (a) A concrete cavity in the bottom slab of the box girder; (b) Near-surface voids in the bearing zone; (c) Insufficient compaction at the base of the pier; (d) Grout leaks due to inadequate sealing of the prestressing cable ducts.

Identifying the extent of such damage is difficult and requires the use of non-destructive methods. One of the ways to identify voids in concrete elements with a high density of near-surface reinforcement and prestressing cables is Ground Penetrating Radar (GPR) testing. This article presents the application of this method using high-frequency antennas to detect anomalies in the structure of hardened concrete in newly built structures.

The authors used the GPR method to assess irregularities in four elements of bridge structures under construction. Identification tests were carried out on the support zone of the girder (Figure 4a), the pier attachment zone (Figure 4b), the lower part of the abutment (Figure 4c) and the piers (Figure 4d).

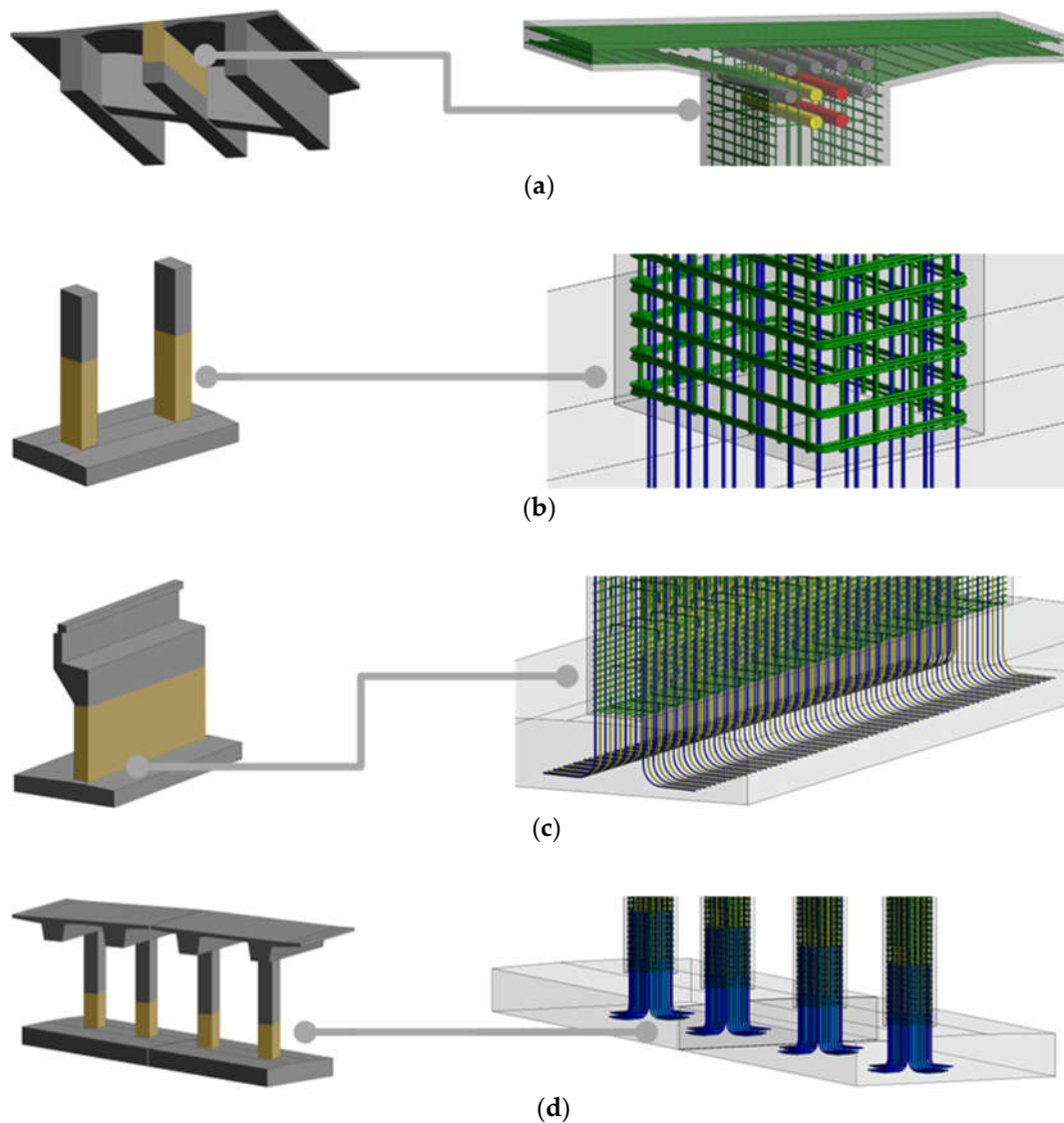


**Figure 4.** Identification tests of selected parts of bridge elements: (a) Support zone of the girder; (b) The pier attachment zone; (c) The lower part of the abutment; (d) The piers.

This research presents in detail an example of irregularities found in the WS-5 viaduct of the right carriageway on the S11 Polish expressway (Figure 5). The structure is a three-span continuous beam made of C50/60 class prestressed concrete. The theoretical spans are  $34.0\text{ m} + 62.0\text{ m} + 34.0\text{ m} = 130.0\text{ m}$ . The skew angle of the structure is variable and ranges from  $32.3^\circ$  to  $39.4^\circ$ . It was designed for class A road load ( $K + 0.3K$ ) according to the Polish Standards (PN). The total width of the structure of the right carriageway is  $15.30\text{ m}$ . There is a one-way road running through the structure,  $12.65\text{ m}$  wide (between the curbs). The superstructure of the viaduct consists of three beams with a rectangular cross-section with an axial spacing of  $4.70\text{ m}$ , connected by a reinforced concrete deck slab with a thickness of at least  $0.25\text{ m}$ . The beams are  $1.20\text{ m}$  wide and have a variable height ranging from  $1.80\text{ m}$  to  $3.50\text{ m}$ . The left cantilever has an overhang of  $1.77\text{ m}$ , while the right one has an overhang of  $2.81\text{ m}$ . Both cantilevers have a variable thickness decreasing from  $0.45\text{ m}$  at the attachment to the girder to  $0.24\text{ m}$  at the ends. In addition to the support crossbeams, a span crossbeam was also designed—one in the extreme spans and one in the central span. The spans are supported by pot bearings, three on each support. The supports consist of two abutments and reinforced concrete piers. The piers were designed as column structures and each intermediate support consists of three columns with a rectangular cross-section. The supports were designed as direct foundations on reinforced ground.

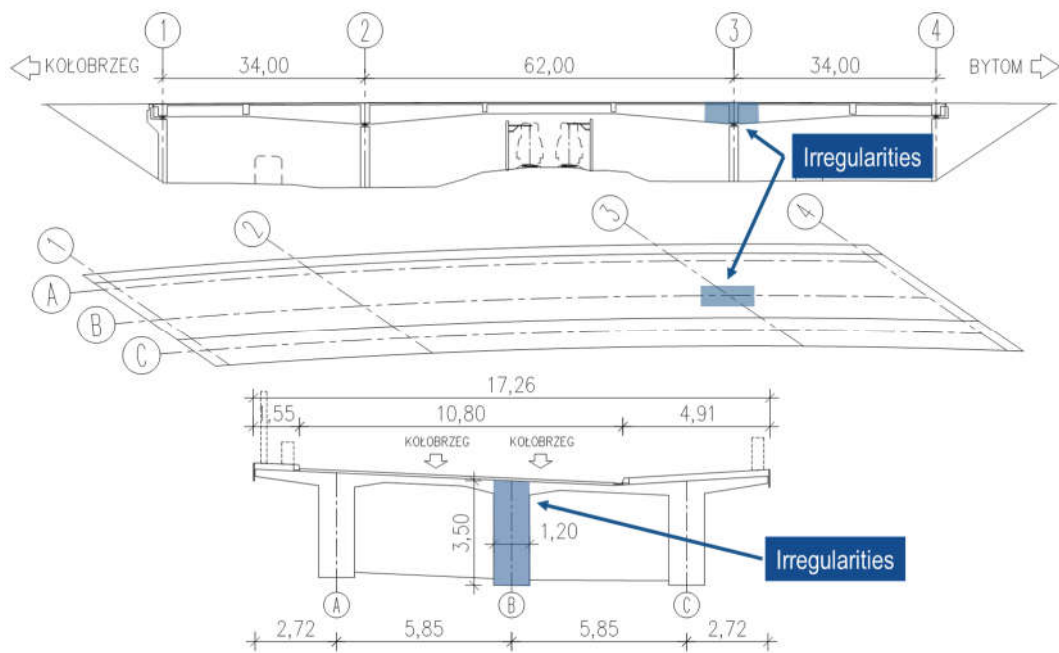


**Figure 5.** Longitudinal section, top view and cross-section with locations of identified irregularities.

During injection works on the right carriageway of the superstructure, irregularities were observed in the internal girder (B) near support No. 3 (Figures 6 and 7). On October 27, 2022, while filling cable duct No. 2, excessive consumption of cement grout was noticed during the injection process. An inspection of the superstructure was carried out immediately and the filling of the adjacent cable ducts (3, 4, 5, 6, 8 and 10) was confirmed. Due to the situation, protective measures were initiated to prevent the cables from being blocked by setting grout. The work involved injecting grout into the cables, which was leaking through the support vents. In this way, it was possible to fill cable ducts 2, 3, 4, 5 and 6. Cables 8 and 10 were not completely filled with grout. The observed increase in pressure above 10 bar made further injection impossible. The work was stopped when the cement consumption reached 575 kg (56%) in cables 8 and 10. After an unsuccessful attempt to inject ducts 8 and 10, moisture was found in the area around the connection of the internal girder with the crossbeam (support 3). Based on the investigation, it was concluded that there was a failure related to the lack of tightness of the prestressing cable sheaths.

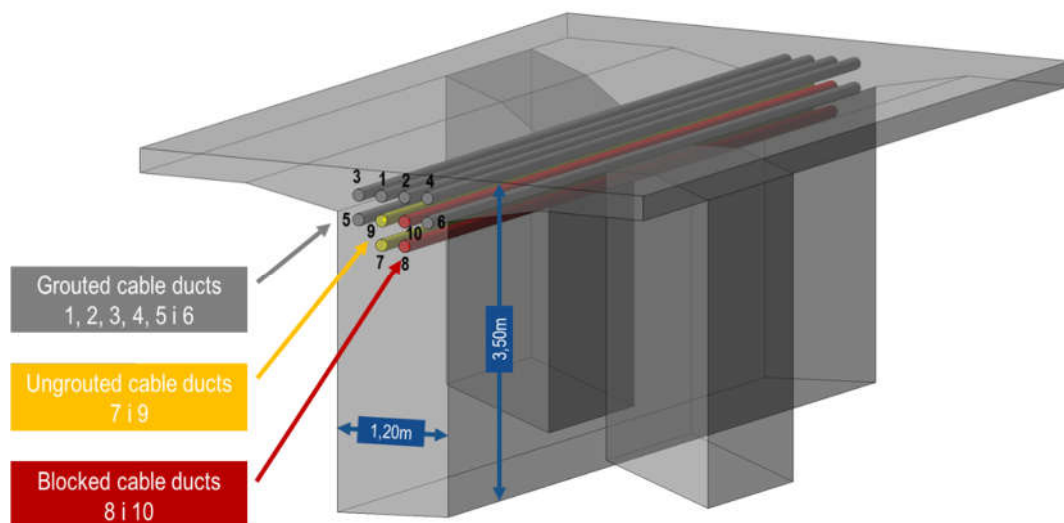


**Figure 6.** Inventory of injection works for girder B in the support axis 3.

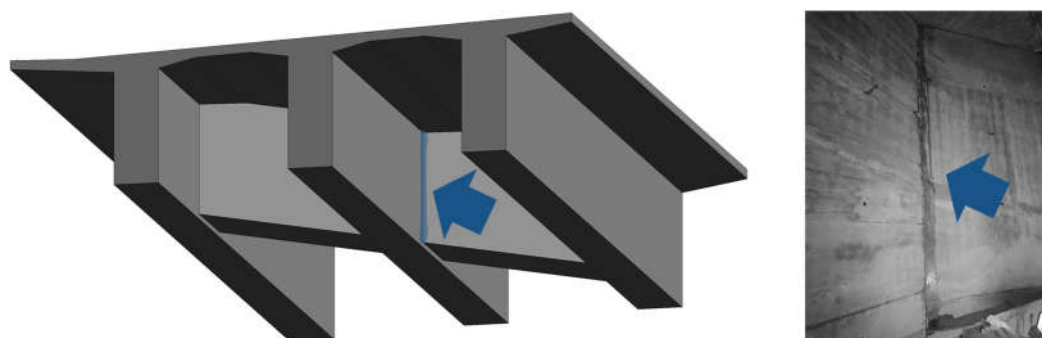


**Figure 7.** Moisture in the area around the connection of the internal girder with the crossbeam (support 3).

Analysis of the documentation related to the arrangement of reinforcement, the location of cable ducts in the support sections and the intersection of the reinforcement from the crossbeams indicates the risk of possible damage to cable sheaths and air vents during concreting. High girders up to 3.50 m in the support cross-section with 10 cables laid in the upper zone together with a high density of reinforcement of the girders and support crossbeams create difficulties during concrete casting (Figure 8). Inserting the rubber pipe while casting the concrete mixture and compacting it with immersion vibrators were the main causes of damage to the prestressing cable sheaths and failure due to their lack of tightness. It should be noted that at this stage it was not possible to clearly determine which of the above factors was the cause of the failure. Nevertheless, it should be clearly stated that the failure was caused by human error during the concreting process of the superstructure. The built-in cable sheaths 8 and 10 have an external diameter of 117 mm and 127 mm, respectively. With a cable axial spacing of 250 mm, the free space for introducing the concrete mixture was 133 mm (second row of cable routes) and 123 mm (third row of cable routes). Photographic documentation confirms the existence of connections between the cable sheaths within the support cross-section, which additionally posed a risk of loss of tightness at the site of the failure.

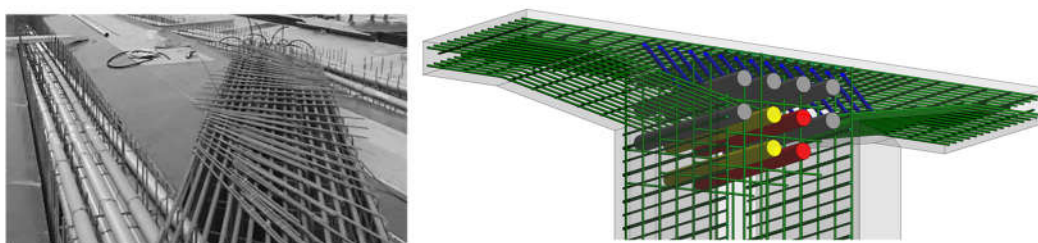


**Figure 8.** The upper zone of the girder above support 3 with difficult access during concreting.

Concreting of the superstructure of the right carriageway of structure WS-5 was divided into two stages. Stage I included concreting the entire central span 2-3 along with part of the outer spans 1-2 and 3-4. Stage II involved concreting the end sections of spans 1-2 and 3-4. Construction joints occurred near the span crossbeams on the side of supports 2 and 3. The concrete mixture was casted using three pumps. Stage I of concreting began on August 3, 2022 at 3:00 a.m. (feeding from pump No. 2) and finished in the early hours of August 4, 2022 at approx. 2:55 a.m. (feeding from pump No. 3). In order to ensure an appropriate rate of mixture delivery, the transport was carried out using 8 concrete trucks from plant No. 1 and 12 concrete trucks from plant No. 2. The maximum allowable time for transport and placement the mixture was up to 120 minutes at an ambient temperature of +15°C, up to 90 minutes at +20°C and up to 30 minutes at ambient temperatures above +30°C.

The concrete mixture was fed from support 1 towards support 4. The layers of the mixture did not exceed the thickness of 50 cm. In order to achieve proper bonding between subsequent layers, the method used required laying the next layer before the freshly laid layer began to set. The concrete mixture was compacted using immersion vibrators. Correct placement and compaction of the mixture without segregation required the pump hose to be inserted between the cable sheaths in the

support zone (Figure 9). At this stage of the work, there was a risk of damaging the cable ducts and vents. A local, unintended horizontal joint formed during the laying of the last layer of the mixture (at the height of the second row of cable ducts) which facilitated the transmission of the grout in the support zone.

The prestressing of the superstructure was performed in two stages. Stage I was carried out from September 7, 2022 to September 13, 2022 and concerned the central span 2-3. Based on the prestressing protocol, the prestressing force resulted in a total elongation at the cable anchors that was below the permissible value of 10%. The actual strength of the concrete in the structure at the moment of prestressing was greater than the required 60 MPa. Stage II was carried out from October 13, 2022 to October 17, 2022 and concerned the extreme spans 1-2 and 3-4. The prestressing protocol confirmed that the actual strength of the concrete in the structure at the moment of prestressing had been corrected to 55.3 MPa (92%). For some cables, in accordance with the designer's guidelines, the tension force was increased to reach a minimum of 90% corrected elongations and maximum strength  $F_{p0,1k} = 6863$  kN.

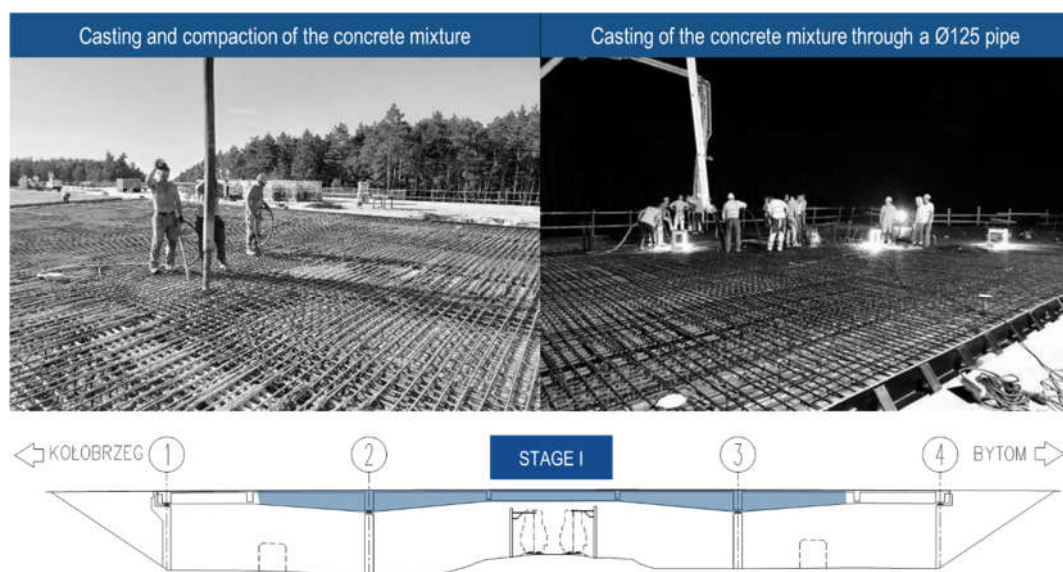


**Figure 9.** Concreting of the right carriageway of the WS-5 superstructure in stage I.

### 3. Description of Method Used in Diagnostics

Diagnosing prestressed bridges with elements that have a high ratio of longitudinal and transverse reinforcement, along with the multi-row tendons layout, is very challenging. Such objects are inherently complex and make drilling, boreholing or other destructive methods impossible or difficult to implement. In these situations, non-destructive testing methods are employed. These methods include magnetic, ground-penetrating radar (GPR), radiological and ultrasonic tests.

The essence of the GPR method is the reception and digital recording of the echo of an electromagnetic wave with a frequency range from 10 MHz to 5-6 GHz, emitted deep into the investigated medium. There are GPR systems with different signal transmission methods, but impulse GPRs are the most commonly used commercially. The electromagnetic wave pulse undergoes reflection, scattering, refraction, and attenuation in the tested medium. The most important phenomenon, from the perspective of the GPR method, is the reflection of a wave at the boundary of two media that differ in their dielectric constants, which is simply expressed as the reflection coefficient  $\Gamma$  according to the equation [67]:

$$\Gamma = \frac{\sqrt{\varepsilon_{r1}} - \sqrt{\varepsilon_{r2}}}{\sqrt{\varepsilon_{r1}} + \sqrt{\varepsilon_{r2}}} \quad (1)$$

where:

$\varepsilon_{r1}, \varepsilon_{r2}$  – relative permittivity of adjacent media.

Distinguishing the boundaries of the medium in the GPR method becomes possible when the power of the reflected signal  $P_r$  is expressed as follows [68,69]:

$$P_r = \left( \frac{\sqrt{\varepsilon_{r1}} - \sqrt{\varepsilon_{r2}}}{\sqrt{\varepsilon_{r1}} + \sqrt{\varepsilon_{r2}}} \right)^2 \geq 0.01 \quad (2)$$

The greater the variation in the relative permittivity of adjacent layers, the higher likelihood of clearly mapping the boundary between them. The relative permittivity of air is 1 and is at least three times lower than in other media. For concrete, the relative permittivity ranges from 3 to 9 [70] corresponding to reflection coefficient values from 0.26 to 0.50, and reflected signal power ranging from 0.07 to 0.25. These parameters are favorable for using the GPR method. Therefore, the presence of empty spaces in anthropogenic forms (concrete honeycombs) makes them clearly visible in GPR images as changes in the amplitude of the recorded reflected wave.

Depending on the antenna parameters and the relative permittivity of the signal propagation media, it is possible to distinguish the boundaries of subsequent layers. The phenomenon of detecting two boundaries reflecting a signal is related to the concept of vertical resolution in the GPR method as described by the equations [69]

$$\Delta d \cong \frac{c}{4f \times \sqrt{\varepsilon_r}} \quad (3)$$

where:

$\Delta d$  – vertical resolution;

$c$  – speed of light;

$f$  – median antenna frequency.

Table 1 shows the calculated values of vertical resolution for three selected antenna frequencies  $f$ , and the relative permittivity for concrete and air (according to formula No. 3). It indicates that antennas above 1 GHz have a theoretical possibility of detecting concrete – void and void – concrete boundaries even when the void is several centimeters thick. The table also includes results for the 600 MHz antenna, which has lower resolution, but is worth using in research. This is because, in concrete structures with significant grain size and reinforcement, antennas with frequencies above 1 GHz may have a limited depth range. Additionally, the signal will be excessively scattered by these structures, potentially making the GPR image excessively noisy, and causing information about concrete honeycombs to blend into the background. The 600 MHz antenna will not be as sensitive to the aforementioned elements due to its lower resolution, which means that significant change in signal amplitude is more likely to be visible in the areas of voids or places with a nonhomogeneous arrangement of aggregates in the concrete.

**Table 1.** Comparison of vertical resolution, antenna frequencies and relative permittivity for concrete and air.

	$f$ [MHz]		
	600	1000	1600
$\varepsilon_r$			
1	0.125	0.075	0.046
3	0.072	0.043	0.027
9	0.041	0.025	0.015

The primary source of information in GPR measurements is the recorded variations in the amplitude of reflected waves. The most commonly used measurement method is reflection profiling. Reflective profiling enables the observation of variations in the distribution of internal structures within the medium and the determination of their depths of occurrence.

Reception and sampling of a single electromagnetic pulse emitted deep into the medium are performed within a time interval defined by the operator, called a *time window*. GPR equipment records the timestamp and value of each *sample*. A group of samples recorded over the entire time window creates a single GPR *trace*. Therefore, a GPR trace is a record of variations in the amplitude

of the received electromagnetic signal over time. Such a single probing record is known as an **A-scan** (Figure 10a).

Subsequent traces are recorded at intervals of time or distance and result in the creation of a GPR record (digital image) called a *radargram*. A radargram generated by moving GPR antennas along the *profile line* represents cross-section of the medium. Such a profile record is known as a **B-scan** (Figure 10b). Several B-scans conducted in a given area at specific intervals enable the generation of **C-scans** (Figure 10c). A C-scan is an "artificial" echogram resulting from the interpolation of information from adjacent B-scans, i.e., a GPR projection generated at various depths below the surface covered by the measurements.

Although the C-scan is the result of interpretation, it carries important information that clearly highlights the interrelation of the phenomena recorded in the B-scans. For this reason, in the chapter describing the results, the research findings are presented in the form of C-scans.

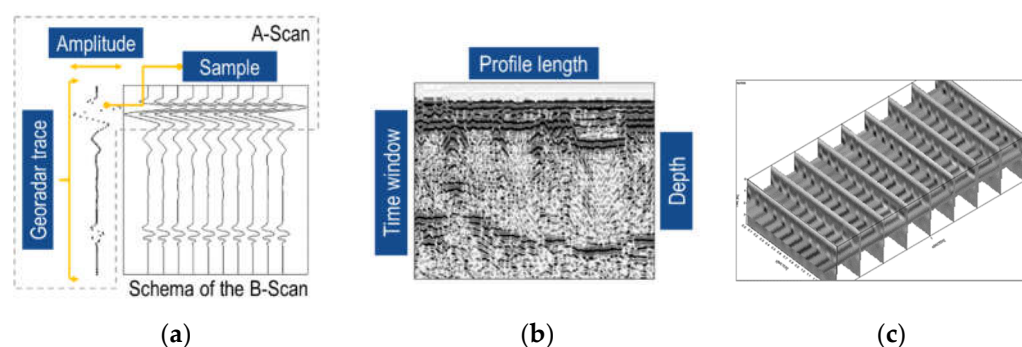


**Figure 10.** Classification of Ground Penetrating Radar (GPR) Data: (a) A-scan and schema of the B-scan; (b) image of the B-scan; (c) C-scan.

#### 4. Results

Identification tests were carried out on February 6, 2023. To detect the anomalies of the hardened concrete structure, measurements of girder B within support 3 were performed. The area was analyzed on three sides (Figure 11):

- **Zone 1** involved the side surface of girder B adjacent to girder C, measuring 4.00 m in length and 1.70 m high;
- **Zone 2** concerned the side surface of girder B adjacent to girder A;
- **Zone 3** included the upper surface of girder B with a length of 10.00 m along the axis of the element.

The GPR method using high-frequency antennas (600 MHz and 1600 MHz) was employed for the research. During the tests, changes in wave amplitude were recorded. Processing the measurement results allowed for the generation of depth GPR cross-sections. These cross-sections formed the basis for interpreting possible structural changes in the studied area.

The performed tests illustrate the zones of structural anomalies in the concrete element, interpreted from 3D models made for each measurement zone separately. The interpretation was based on maps and the horizontal cuts from selected depths in the model. These depths correspond to the maximum extent of the anomaly zone identified in a model, that is, the anomaly may start slightly higher and disappear slightly deeper. The generated 3D models in zones 1 and 2 were created from longitudinal profiles. In the upper zone 3, the examined area was covered with a dense measurement grid. Longitudinal profiles (PD) were made along the axis of the girder, spaced every 0.2 m, and transverse profiles (PP) were made perpendicular to the axis of the object, spaced every 0.3 m. Based on these, two separate, independent 3D models were created. Typically, models are made by overlapping all profiles. In this case, such a procedure was intentionally avoided to prevent duplication and amplification of interference zones, e.g. from reinforcement.

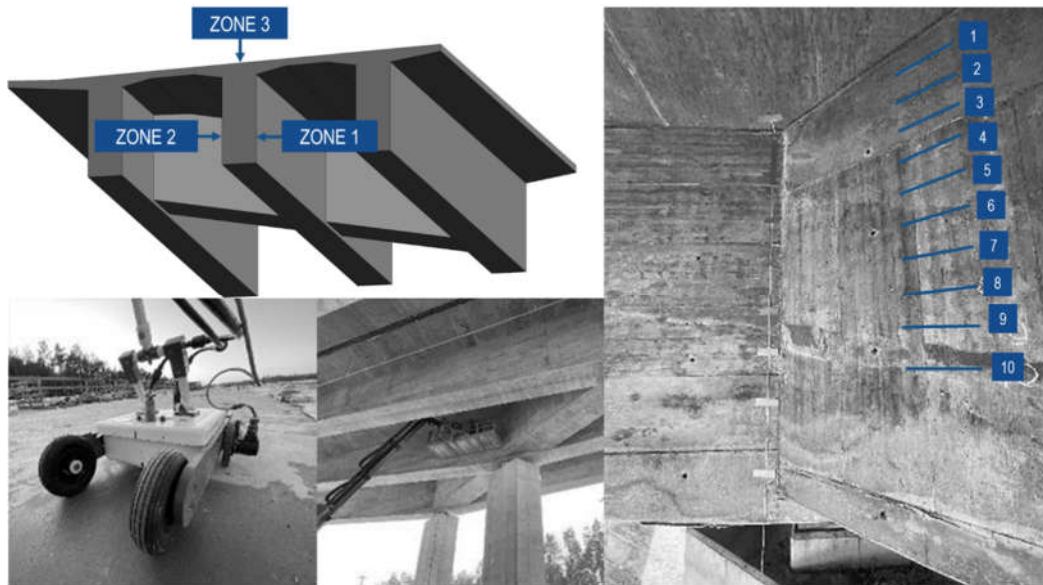


**Figure 11.** Identification tests during a site inspection with marked reference lines.

The interpretation involved selecting zones exhibiting a significant increase in the absolute amplitude of the signal, which usually corresponded to changes in the structure of the tested object. In the analyzed case, these could also be zones corresponding to a large accumulation and density of intersecting reinforcement within the tested structural element, formwork elements or elements of prestressing cables as well as areas filled with cement grout. Tests on such elements are extremely difficult to interpret due to the large amount of reinforcement, steel formwork elements, and the additional presence of prestressing cables. Changes in the concrete structure identified during the test, related to insufficient vibration of the concrete or its separation (distribution of aggregate in the hardened cement slurry) are shown in Figures 12, 13, and 14.

In all generated cross-sections, the extent of irregularities in the concrete structure was marked, along with the depth of occurrence. Based on the identification tests carried out on girder B within support 3 for data from the 600 MHz and 1600 MHz antennas, it was found that there were anomaly zones, i.e. irregularities in the concrete structure related to insufficient vibration and separation of the mixture. In the side zones (1 and 2), anomalies related to local changes in the concrete structure were found. The generated depth sections confirmed the occurrence of an area of structural deviations at a depth of up to 0.22 m in zone 1 and up to 0.54 m in zone 2. Anomalies were also found in zone 3 where the irregularities in the concrete structure occurred at a depth of up to 0.71 m in the vicinity of the intermediate support on the side of support 4. Additionally, at a depth of up to 0.05 m, irregularities were found in the area of the support vents. The observed concrete structure anomalies required additional verification consisting in control drilling in representative areas.

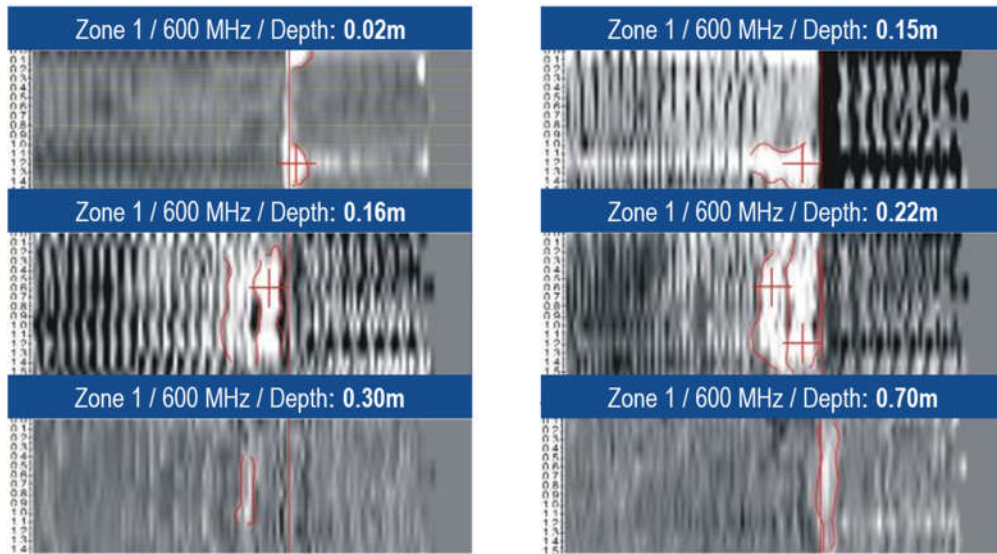


**Figure 12.** Generated cross-sections in zone 1 from longitudinal profiles for a 600 MHz antenna.

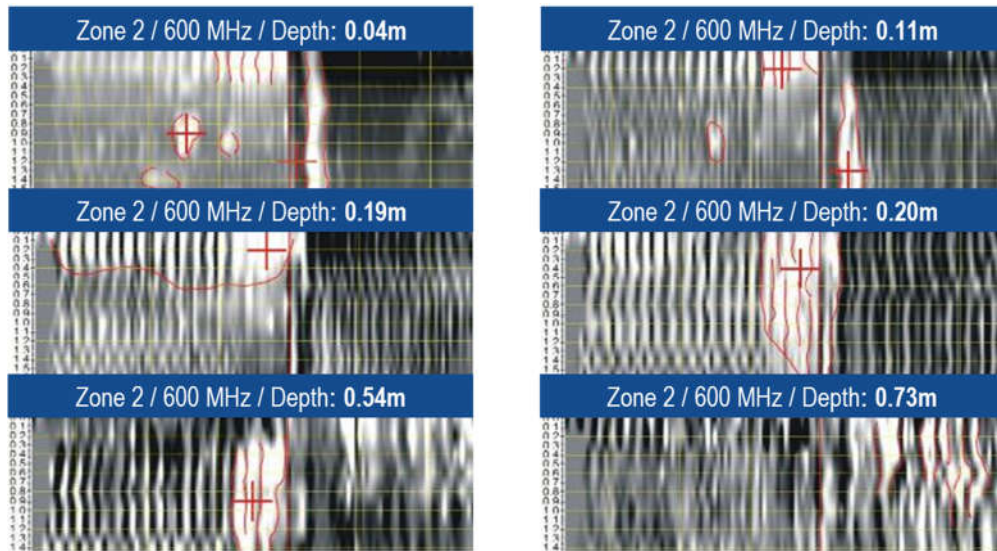


**Figure 13.** Generated cross-sections in zone 2 from longitudinal profiles for a 600 MHz antenna.

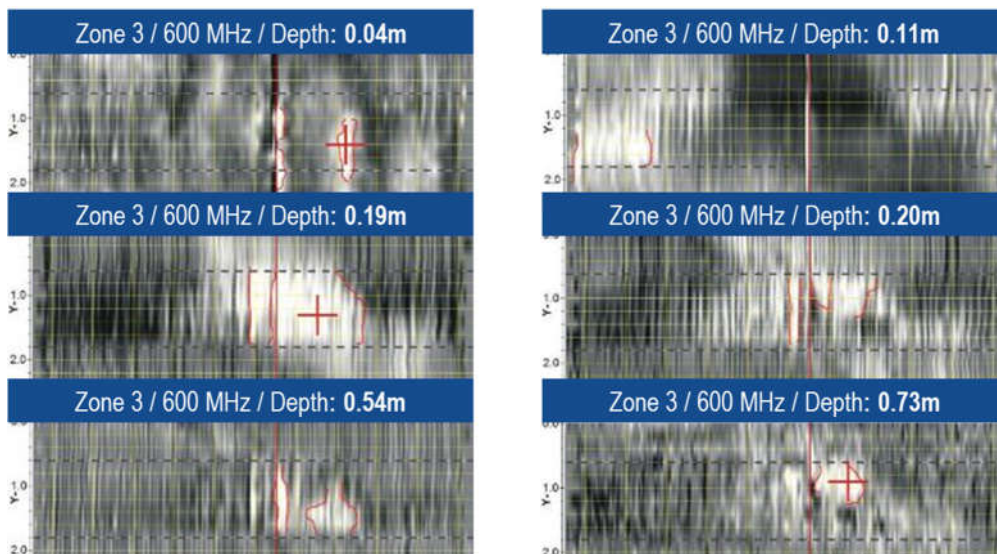


**Figure 14.** Generated cross-sections in zone 3 from longitudinal profiles for a 600 MHz antenna.

## 5. Discussion

Based on GPR identification tests, the occurrence of anomalies related to local irregularities in the concrete structure in girder B was confirmed. In order to fully assess these irregularities, three control drillings were performed using a drill bit with a diameter of 50 mm and a depth of up to 250 mm for horizontal points and up to 150 mm for vertical points. The locations of the boreholes are shown in Figure 15. Based on the drillings, it was determined that the anomalies identified using the GPR method are associated with local imperfections in the concrete structure and rule out the presence of concrete voids. Examination of the collected samples confirmed the occurrence of isolated internal concrete honeycombs up to 5 mm attributed to insufficient vibration of the concrete and non-uniform distribution of aggregate in the hardened cement slurry due to segregation of the mixture during concreting. The identified concrete structural anomalies are a common technological phenomenon and do not affect the load-bearing capacity and durability of the structure.

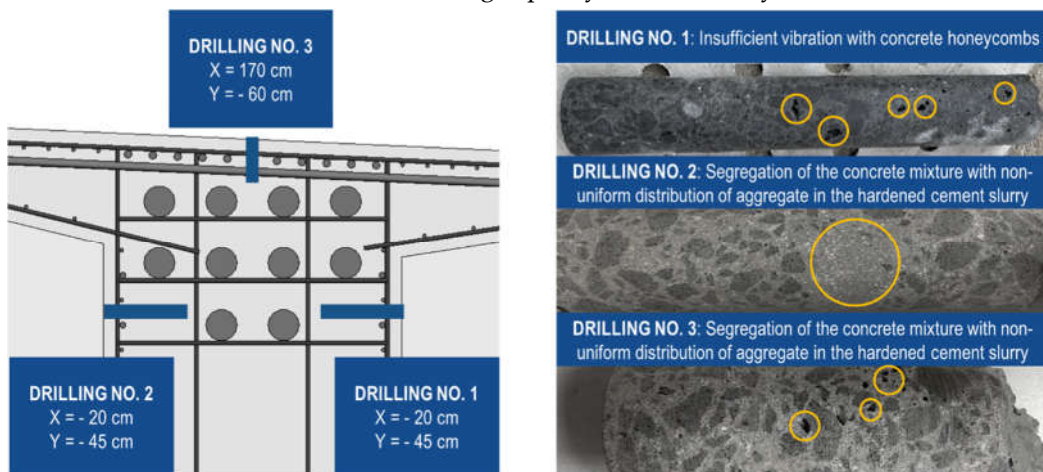


**Figure 15.** Control drillings.

Taking into account the results of tests identifying the type and scope of irregularities in the concrete structure at the locations where cable sheath leaks occurred, it was decided to implement a repair program involving supplementary injection. In order to fully inject cables No. 8 and 10, it was necessary to gain access to the cable sheath zones through hydro-cutting at selected places. Then, from the inspection windows, the patency of the sheaths was checked using compressed air and an endoscopic camera (Figure 16). After confirming the extent of the injection discontinuity of the cables and the reach of the injection mortar, additional injection was initiated using the inspection window. The entire work required air-tight sealing of cable ducts with injection power supply and venting installations, as well as reconstruction of the concrete of the inspection windows.



**Figure 16.** Implementation of the supplementary injection program.

## 6. Conclusions

The usefulness of the GPR method in non-invasive diagnostics of complex prestressed structures significantly influences the scope and type of repair programs. Thanks to the obtained images, we are able to determine the location and extent of irregularities in the structure of hardened concrete. Based on this information, the type of irregularities can be verified using an invasive method through selected control drillings and the presence of concrete voids can be excluded.

Taking into account the identification tests carried out and the analysis of the design and construction documentation, it was possible to assess the occurrence of grout leakage into adjacent channels. This leakage was caused by the lack of tightness in the prestressing cable sheaths. It was deemed appropriate to suspend further action until the underlying causes were clarified. The resulting situation threatened the durability of inadequately injected prestressing cables and necessitated the implementation of an effective repair program. During the inspection of the cable ducts, it was confirmed that the work performed was correct, thereby excluding any irregularities at this stage of the work. Local damage to the cable sheaths occurred during concreting. Inserting a rubber pipe while feeding the concrete mixture or compacting with immersion vibrators resulted in leaks in the prestressing cables sheaths and air vents. This was confirmed by the nature of the failure and the location where it occurred. No irregularities were found during the prestressing of the structure, so there was no risk of reducing the load-bearing capacity of the structure.

Moisture in the area around the connection of girder with the crossbeam in the axis of support 3 occurred as a result of injection and a pressure increase above 10 bar. The presence of moisture was related to grout penetrating through leaky cable sheaths, causing the filling of non-vibrated spaces within the concrete structure. The outflow of grout from the adjacent support vents, observed during the injection works, was caused by their prior damage along with the cable sheaths in this area and the transmission of grout through the horizontal, apparent and local joints between the built-in layers of the mixture.

Identification tests carried out on girder B in the site of the failure confirmed the occurrence of local irregularities in the concrete structure related to inadequate vibration and separation of the mixture. These irregularities were verified through control drilling which confirmed the presence of internal concrete honeycombs up to 5 mm and uneven distribution of aggregate in the hardened cement slurry. The identified concrete structure anomalies are a common technological phenomenon in the construction of monolithic concrete elements and do not affect the load-bearing capacity and durability of the structure. The completed supplementary injection repair program ensured the durability of the structure.

**Author Contributions:** Conceptualization, P.L. and Ł.O.; methodology, Ł.O.; software, Ł.O.; validation, M.J. and D.P.; formal analysis, P.L. and Ł.O.; investigation, M.J. and M.U.; resources, M.J., D.P. and M.U.; data curation, D.P.; writing—original draft preparation, P.L., M.J., M.U., D.P. and Ł.O.; writing—review and editing, P.L., M.J., M.U., D.P. and Ł.O.; visualization, P.L., M.J., M.U., D.P. and Ł.O.; supervision, M.J.; project administration, D.P.; funding acquisition, D.P. All authors have read and agreed to the published version of the manuscript.”

**Funding:** This research was funded by grant number BKM/505/RB-5/2024 obtained at the Silesian University of Technology (Poland) by Dawid Piotrowski.

**Data Availability Statement:** Dataset available on request from the authors.

**Conflicts of Interest:** The authors declare no conflicts of interest.

## References

1. Gagg, C.R. Cement and Concrete as an Engineering Material: An Historic Appraisal and Case Study Analysis. *Eng Fail Anal* **2014**, *40*, 114–140, doi:10.1016/j.engfailanal.2014.02.004.
2. Rosa, A.C.; Hammad, A.W.A.; Boer, D.; Haddad, A. Use of Operational Research Techniques for Concrete Mix Design: A Systematic Review. *Heliyon* **2023**, *9*, e15362, doi:10.1016/j.heliyon.2023.e15362.

3. Shafiei Dastgerdi, A.; Peterman, R.J.; Riding, K.; Beck, B.T. Effect of Concrete Mixture Components, Proportioning, and Compressive Strength on Fracture Parameters. *Constr Build Mater* **2019**, *206*, 179–192, doi:10.1016/j.conbuildmat.2019.02.025.
4. Lantsoght, E.O.L. Advanced Structural Concrete Materials in Bridges. *Materials* **2022**, *15*, 8346, doi:10.3390/ma15238346.
5. Kumar Sahu, P. Defects in Concrete in Building Construction. *Journal of Advances in Geotechnical Engineering* **2022**, *5*, 1–9, doi:10.5281/zenodo.7193395.
6. Krzywoń, R.; Hulimka, J. Common Defects of Prefabricated Prestressed Elements for Industrial Construction. *Buildings* **2024**, *14*, 673, doi:10.3390/buildings14030673.
7. Breyse, D. Nondestructive Evaluation of Concrete Strength: An Historical Review and a New Perspective by Combining NDT Methods. *Constr Build Mater* **2012**, *33*, 139–163, doi:10.1016/j.conbuildmat.2011.12.103.
8. Hoła, J.; Bień, J.; Sadowski, Ł.; Schabowicz, K. Non-Destructive and Semi-Destructive Diagnostics of Concrete Structures in Assessment of Their Durability. *Bulletin of the Polish Academy of Sciences Technical Sciences* **2015**, *63*, 87–96, doi:10.1515/bpasts-2015-0010.
9. Kot, P.; Muradov, M.; Gkantou, M.; Kamaris, G.S.; Hashim, K.; Yeboah, D. Recent Advancements in Non-Destructive Testing Techniques for Structural Health Monitoring. *Applied Sciences* **2021**, *11*, 2750, doi:10.3390/app11062750.
10. Ottosen, L.M.; Kunther, W.; Ingeman-Nielsen, T.; Karatosun, S. Non-Destructive Testing for Documenting Properties of Structural Concrete for Reuse in New Buildings: A Review. *Materials* **2024**, *17*, 3814, doi:10.3390/ma17153814.
11. Boccacci, G.; Frasca, F.; Bertolin, C.; Siani, A.M. Diagnosis of Historic Reinforced Concrete Buildings: A Literature Review of Non-Destructive Testing (NDT) Techniques. *Procedia Structural Integrity* **2024**, *55*, 160–167, doi:10.1016/j.prostr.2024.02.021.
12. Pucinotti, R. Reinforced Concrete Structure: Non Destructive in Situ Strength Assessment of Concrete. *Constr Build Mater* **2015**, *75*, 331–341, doi:10.1016/j.conbuildmat.2014.11.023.
13. Hussain, A.; Akhtar, S. Review of Non-Destructive Tests for Evaluation of Historic Masonry and Concrete Structures. *Arab J Sci Eng* **2017**, *42*, 925–940, doi:10.1007/s13369-017-2437-y.
14. Venkatesh, P.; Alapati, M. Condition Assessment of Existing Concrete Building Using Non-Destructive Testing Methods for Effective Repair and Restoration-A Case Study. *Civil Engineering Journal* **2017**, *3*, 841, doi:10.28991/cej-030919.
15. Dixit, M.; Gupta, A.K. A Review of Different Assessment Methods of Corrosion of Steel Reinforcement in Concrete. *Iranian Journal of Science and Technology, Transactions of Civil Engineering* **2022**, *46*, 735–752, doi:10.1007/s40996-021-00644-5.
16. Golewski, G.L. The Phenomenon of Cracking in Cement Concretes and Reinforced Concrete Structures: The Mechanism of Cracks Formation, Causes of Their Initiation, Types and Places of Occurrence, and Methods of Detection—A Review. *Buildings* **2023**, *13*, 765, doi:10.3390/buildings13030765.
17. Santini, S.; Forte, A.; Sguerri, L. The Structural Diagnosis of Existing RC Buildings: The Role of Nondestructive Tests in the Case of Low Concrete Strength. *Infrastructures (Basel)* **2020**, *5*, 100, doi:10.3390/infrastructures5110100.
18. Köliö, A.; Pakkala, T.A.; Hohti, H.; Laukkarinen, A.; Lahdensivu, J.; Mattila, J.; Pentti, M. The Corrosion Rate in Reinforced Concrete Facades Exposed to Outdoor Environment. *Mater Struct* **2017**, *50*, 23, doi:10.1617/s11527-016-0920-7.
19. Lachowicz, J.; Rucka, M. Application of GPR Method in Diagnostics of Reinforced Concrete Structures. *Diagnostyka* **2015**, *16*, 31–36.
20. Milovanović, B.; Banjad Pečur, I. Review of Active IR Thermography for Detection and Characterization of Defects in Reinforced Concrete. *J Imaging* **2016**, *2*, 11, doi:10.3390/jimaging2020011.
21. McCann, D.M.; Forde, M.C. Review of NDT Methods in the Assessment of Concrete and Masonry Structures. *NDT & E International* **2001**, *34*, 71–84, doi:10.1016/S0963-8695(00)00032-3.
22. Faris, N.; Zayed, T.; Abdelkader, E.M.; Fares, A. Corrosion Assessment Using Ground Penetrating Radar in Reinforced Concrete Structures: Influential Factors and Analysis Methods. *Autom Constr* **2023**, *156*, 105130, doi:10.1016/j.autcon.2023.105130.
23. Hussein, R.; Etete, B.; Mahdi, H.; Al-Shukri, H. Detection and Delineation of Cracks and Voids in Concrete Structures Using the Ground Penetrating Radar Technique. *J Appl Geophy* **2024**, *226*, 105379, doi:10.1016/j.jappgeo.2024.105379.
24. Dérobert, X.; Villain, G. Effect of Water and Chloride Contents and Carbonation on the Electromagnetic Characterization of Concretes on the GPR Frequency Band through Designs of Experiment. *NDT & E International* **2017**, *92*, 187–198, doi:10.1016/j.ndteint.2017.09.001.
25. Kaplanvural, İ. Volumetric Water Content Estimation of Concrete by Particle Swarm Optimization of GPR Data. *Constr Build Mater* **2023**, *375*, 130995, doi:10.1016/j.conbuildmat.2023.130995.
26. Tešić, K.; Baričević, A.; Serdar, M. Non-Destructive Corrosion Inspection of Reinforced Concrete Using Ground-Penetrating Radar: A Review. *Materials* **2021**, *14*, 975, doi:10.3390/ma14040975.

27. Faris, N.; Zayed, T.; Fares, A.; Abdelkhalik, S.; Abdelkader, E.M. Automated Rebar Recognition and Corrosion Assessment of Concrete Bridge Decks Using Ground Penetrating Radar. *Autom Constr* **2024**, *166*, 105631, doi:10.1016/j.autcon.2024.105631.
28. Hong, S.; Mo, G.; Song, S.; Li, D.; Huang, Z.; Hou, D.; Chen, H.; Mao, X.; Lou, X.; Dong, B. Research on Reinforcement Corrosion Detection Method Based on the Numerical Simulation of Ground-Penetrating Radar.
29. Kuchipudi, S.T.; Ghosh, D.; Gupta, H. Automated Assessment of Reinforced Concrete Elements Using Ground Penetrating Radar. *Autom Constr* **2022**, *140*, 104378, doi:10.1016/j.autcon.2022.104378.
30. Wang, Y.; Qin, H.; Miao, F. A Multi-Path Encoder Network for GPR Data Inversion to Improve Defect Detection in Reinforced Concrete. *Remote Sens (Basel)* **2022**, *14*, 5871, doi:10.3390/rs14225871.
31. Hu, H.; Fang, H.; Wang, N.; Ma, D.; Dong, J.; Li, B.; Di, D.; Zheng, H.; Wu, J. Defects Identification and Location of Underground Space for Ground Penetrating Radar Based on Deep Learning. *Tunnelling and Underground Space Technology* **2023**, *140*, 105278, doi:10.1016/j.tust.2023.105278.
32. Wong, P.T.; Lai, W.W.; Poon, C. Classification of Concrete Corrosion States by GPR with Machine Learning. *Constr Build Mater* **2023**, *402*, 132855, doi:10.1016/j.conbuildmat.2023.132855.
33. Abu Dabous, S.; Yaghi, S.; Alkass, S.; Moselhi, O. Concrete Bridge Deck Condition Assessment Using IR Thermography and Ground Penetrating Radar Technologies. *Autom Constr* **2017**, *81*, 340–354, doi:10.1016/j.autcon.2017.04.006.
34. Solla, M.; Lagüela, S.; Fernández, N.; Garrido, I. Assessing Rebar Corrosion through the Combination of Nondestructive GPR and IRT Methodologies. *Remote Sens (Basel)* **2019**, *11*, 1705, doi:10.3390/rs11141705.
35. Jankú, M.; Cikrle, P.; Grošek, J.; Anton, O.; Stryk, J. Comparison of Infrared Thermography, Ground-Penetrating Radar and Ultrasonic Pulse Echo for Detecting Delaminations in Concrete Bridges. *Constr Build Mater* **2019**, *225*, 1098–1111, doi:10.1016/j.conbuildmat.2019.07.320.
36. Yang, X.; Huang, R.; Meng, Y.; Liang, J.; Rong, H.; Liu, Y.; Tan, S.; He, X.; Feng, Y. Overview of the Application of Ground-Penetrating Radar, Laser, Infrared Thermal Imaging, and Ultrasonic in Nondestructive Testing of Road Surface. *Measurement* **2024**, *224*, 113927, doi:10.1016/j.measurement.2023.113927.
37. Kang, S.; Yu, J.-D.; Han, W.; Lee, J.-S. Nondestructive Detection of Cavities beneath Concrete Plates Using Ground Penetrating Radar and Microphone. *NDT & E International* **2022**, *130*, 102663, doi:10.1016/j.ndteint.2022.102663.
38. Lai, W.W.L.; Leong-Ying Ho, M.; Chang, R.K.W.; Sham, J.F.C.; Poon, C.-S. Tracing and Imaging Minor Water Seepage of Concealed PVC Pipe in a Reinforced Concrete Wall by High-Frequency Ground Penetrating Radar. *Constr Build Mater* **2017**, *151*, 840–847, doi:10.1016/j.conbuildmat.2017.06.148.
39. Garrido, I.; Solla, M.; Lagüela, S.; Fernández, N. IRT and GPR Techniques for Moisture Detection and Characterisation in Buildings. *Sensors* **2020**, *20*, 6421, doi:10.3390/s20226421.
40. Buliuk, V.; Ihamouten, A.; Heinkele, C.; Dérobert, X. A Global Approach to Detecting and Characterizing Water Leakage in a Concrete Bridge Deck: Parametric Study to Validate an Adapted Full-Waveform Inversion Method. *Transportation Engineering* **2024**, 100283, doi:10.1016/j.treng.2024.100283.
41. Tasker, L.; Karrech, A.; Shragge, J.; Josh, M. Time-Lapse Monitoring of Internal Alteration of a Concrete Structure Using Ground Penetrating Radar. *Constr Build Mater* **2018**, *191*, 300–310, doi:10.1016/j.conbuildmat.2018.10.008.
42. Liang, X.; Yu, X.; Jin, Y.; Huang, J. Compactness Prediction of Asphalt Concrete Using Ground-Penetrating Radar: A Comparative Study. *Constr Build Mater* **2022**, *361*, 129588, doi:10.1016/j.conbuildmat.2022.129588.
43. Kahil, N.S.; Tempe, V.; Yeferni, A.; Calon, N.; Benkhelfallah, Z.; Annag, I.; Mbongo, G. Automatic Analysis of Railway Ground Penetrating Radar: Using Signal Processing and Machine Learning Approaches to Assess Railroad Track Substructure. *Transportation Research Procedia* **2023**, *72*, 3008–3015, doi:10.1016/j.trpro.2023.11.848.
44. Kumar, V.; Morris, I.M.; Lopez, S.A.; Glisic, B. Identifying Spatial and Temporal Variations in Concrete Bridges with Ground Penetrating Radar Attributes. *Remote Sens (Basel)* **2021**, *13*, 1846, doi:10.3390/rs13091846.
45. Boldrin, P.; Fornasari, G.; Rizzo, E. Review of Ground Penetrating Radar Applications for Bridge Infrastructures. *NDT* **2024**, *2*, 53–75, doi:10.3390/ndt2010004.
46. Harseno, R.W.; Lee, S.-J.; Kee, S.-H.; Kim, S. Evaluation of Air-Cavities behind Concrete Tunnel Linings Using GPR Measurements. *Remote Sens (Basel)* **2022**, *14*, 5348, doi:10.3390/rs14215348.
47. Yang, S.; Wang, Z.; Wang, J.; Cohn, A.G.; Zhang, J.; Jiang, P.; Nie, L.; Sui, Q. Defect Segmentation: Mapping Tunnel Lining Internal Defects with Ground Penetrating Radar Data Using a Convolutional Neural Network. *Constr Build Mater* **2022**, *319*, 125658, doi:10.1016/j.conbuildmat.2021.125658.
48. Liu, B.; Zhang, J.; Lei, M.; Yang, S.; Wang, Z. Simultaneous Tunnel Defects and Lining Thickness Identification Based on Multi-Tasks Deep Neural Network from Ground Penetrating Radar Images. *Autom Constr* **2023**, *145*, 104633, doi:10.1016/j.autcon.2022.104633.

49. Bigman, D.P.; Day, D.J. Ground Penetrating Radar Inspection of a Large Concrete Spillway: A Case-Study Using SFCW GPR at a Hydroelectric Dam. *Case Studies in Construction Materials* **2022**, *16*, e00975, doi:10.1016/j.cscm.2022.e00975.
50. Gereá, A.G.; Mihai, A.E. Exploring the Ground-Penetrating Radar Technique's Effectiveness in Diagnosing Hydropower Dam Crest Conditions: Insights from Gura Apelor and Herculane Dams, Romania. *Applied Sciences* **2024**, *14*, 7212, doi:10.3390/app14167212.
51. Ma, C.; Zhao, W.; Li, G.; Liu, J.; Deng, J.; Ding, W. The Ground Penetrating Radar Response Recognition of Hidden Dam Defects Using Multi-Output Convolutional Neural Network. *J Appl Geophys* **2024**, *225*, 105397, doi:10.1016/j.jappgeo.2024.105397.
52. Sun, H.; Pashoutani, S.; Zhu, J. Nondestructive Evaluation of Concrete Bridge Decks with Automated Acoustic Scanning System and Ground Penetrating Radar. *Sensors* **2018**, *18*, 1955, doi:10.3390/s18061955.
53. Peng, M.; Wang, D.; Liu, L.; Shi, Z.; Shen, J.; Ma, F. Recent Advances in the GPR Detection of Grouting Defects behind Shield Tunnel Segments. *Remote Sens (Basel)* **2021**, *13*, 4596, doi:10.3390/rs13224596.
54. Wu, X.; Bao, X.; Shen, J.; Chen, X.; Cui, H. Evaluation of Void Defects behind Tunnel Lining through GPR Forward Simulation. *Sensors* **2022**, *22*, 9702, doi:10.3390/s22249702.
55. Zatar, W.; Nghiem, H.; Nguyen, H. Detecting Reinforced Concrete Rebars Using Ground Penetrating Radars. *Applied Sciences* **2024**, *14*, 5808, doi:10.3390/app14135808.
56. Dinh, K.; Gucunski, N.; Duong, T.H. Migration-Based Automated Rebar Picking for Condition Assessment of Concrete Bridge Decks with Ground Penetrating Radar. *NDT & E International* **2018**, *98*, 45–54, doi:10.1016/j.ndteint.2018.04.009.
57. Elliott, J.B.; Chaney, D.; Murtaza, H. Angled Ground Penetrating Radar to Detect and Position Reinforcement and Bearing Lengths within Reinforced Autoclaved Aerated Concrete Planks. *Constr Build Mater* **2024**, *449*, doi:10.1016/j.conbuildmat.2024.138528.
58. Lachowicz, J.; Rucka, M. 3-D Finite-Difference Time-Domain Modelling of Ground Penetrating Radar for Identification of Rebars in Complex Reinforced Concrete Structures. *Archives of Civil and Mechanical Engineering* **2018**, *18*, 1228–1240, doi:10.1016/j.acme.2018.01.010.
59. Liu, H.; Lin, C.; Cui, J.; Fan, L.; Xie, X.; Spencer, B.F. Detection and Localization of Rebar in Concrete by Deep Learning Using Ground Penetrating Radar. *Autom Constr* **2020**, *118*, 103279, doi:10.1016/j.autcon.2020.103279.
60. Alam, A.N.; Reinhart, W.F.; Napolitano, R.K. Data-Driven Evaluation of Building Materials Using Ground Penetrating Radar. *Journal of Building Engineering* **2024**, *95*, 110188, doi:10.1016/j.job.2024.110188.
61. Yoon, S.; Son, S.; Kim, S. Design, Construction, and Curing Integrated Management of Defects in Finishing Works of Apartment Buildings. *Sustainability* **2021**, *13*, 5382, doi:10.3390/su13105382.
62. Luo, H.; Lin, L.; Chen, K.; Antwi-Afari, M.F.; Chen, L. Digital Technology for Quality Management in Construction: A Review and Future Research Directions. *Developments in the Built Environment* **2022**, *12*, 100087, doi:10.1016/j.dibe.2022.100087.
63. Rasol, M.A.; Pérez-Gracia, V.; Solla, M.; Pais, J.C.; Fernandes, F.M.; Santos, C. An Experimental and Numerical Approach to Combine Ground Penetrating Radar and Computational Modeling for the Identification of Early Cracking in Cement Concrete Pavements. *NDT & E International* **2020**, *115*, 102293, doi:10.1016/j.ndteint.2020.102293.
64. Hasan, Md.I.; Yazdani, N. Ground Penetrating Radar Utilization in Exploring Inadequate Concrete Covers in a New Bridge Deck. *Case Studies in Construction Materials* **2014**, *1*, 104–114, doi:10.1016/j.cscm.2014.04.003.
65. Liu, H.; Zhong, J.; Ding, F.; Meng, X.; Liu, C.; Cui, J. Detection of Early-Stage Rebar Corrosion Using a Polarimetric Ground Penetrating Radar System. *Constr Build Mater* **2022**, *317*, 125768, doi:10.1016/j.conbuildmat.2021.125768.
66. Zhao, S.; Al-Qadi, I.L.; Wang, S. Prediction of Thin Asphalt Concrete Overlay Thickness and Density Using Nonlinear Optimization of GPR Data. *NDT & E International* **2018**, *100*, 20–30, doi:10.1016/j.ndteint.2018.08.001.
67. Reynolds, J.M. *An Introduction to Applied and Environmental Geophysics*; 2nd Edition.; Wiley-Blackwell, 2011; ISBN 978-0-471-48536-0.
68. Annan, A.P. *Ground Penetrating Radar*; Canada, 2000;
69. Annan, A.P. *Ground Penetrating Radar*; Canada, 2001;
70. Karczewski, J.; Ortyl, Ł.; Pasternak, M. *Zarys Metody Georadarowej*; 2nd Edition.; Wydawnictwa AGH: Kraków, 2011; ISBN 978-83-7464-422-8.

**Disclaimer/Publisher's Note:** The statements, opinions and data contained in all publications are solely those of the individual author(s) and contributor(s) and not of MDPI and/or the editor(s). MDPI and/or the editor(s) disclaim responsibility for any injury to people or property resulting from any ideas, methods, instructions or products referred to in the content.